The Astrophysical Journal, 720:1405–1416, 2010 September 10 doi:10.1088/0004-637X/720/2/1405

SOLAR MAGNETIC TRACKING. III. APPARENT UNIPOLAR FLUX EMERGENCE IN HIGH-RESOLUTION OBSERVATIONS

D. A. Lamb[1], C. E. DeForest[2], H. J. Hagenaar[3], C. E. Parnell[4], and B. T. Welsch[5]
[1] Catholic University of America, NASA Goddard Space Flight Center, Code 671, Greenbelt, MD 20771, USA; dlamb@spd.aas.org
[2] Southwest Research Institute, 1050 Walnut Street Suite 300, Boulder, CO 80302, USA
[3] Lockheed Martin Advanced Technology Center, Org. ADBS, Bldg 252, Palo Alto, CA 94304, USA
[4] School of Mathematics and Statistics, University of St. Andrews, St. Andrews, Scotland, KY16 9SS, UK
[5] University of California, Berkeley Space Sciences Laboratory, 7 Gauss Way, Berkeley, CA 94720, USA
Received 2010 February 11; accepted 2010 July 10; published 2010 August 23

ABSTRACT

Understanding the behavior of weak magnetic fields near the detection limit of current instrumentation is important for determining the flux budget of the solar photosphere at small spatial scales. Using 0.″3-resolution magnetograms from the Solar Optical Telescope's Narrowband Filter Imager (NFI) on the *Hinode* spacecraft, we confirm that the previously reported apparent unipolar magnetic flux emergence seen in intermediate-resolution magnetograms is indeed the coalescence of previously existing flux. We demonstrate that similar but smaller events seen in NFI magnetograms are also likely to correspond to the coalescence of previously existing weak fields. The uncoalesced flux, detectable only in the ensemble average of hundreds of these events, accounts for 50% of the total flux within 3 Mm of the detected features. The spatial scale at which apparent unipolar emergence can be directly observed as coalescence remains unknown. The polarity of the coalescing flux is more balanced than would be expected given the imbalance of the data set, however without further study we cannot speculate whether this implies that the flux in the apparent unipolar emergence events is produced by a granulation-scale dynamo or is recycled from existing field.

Key words: Sun: granulation – Sun: photosphere – Sun: surface magnetism

Online-only material: color figures

1. INTRODUCTION

Understanding the behavior and distribution of magnetic fields near the detection limit of current instrumentation is important for determining the flux budget of the solar photosphere at small spatial scales. Since 2006, the Solar Optical Telescope (SOT; Tsuneta et al. 2008) on the *Hinode* spacecraft (Kosugi et al. 2007) has made routinely available relatively long-duration data sets of the solar photosphere and chromosphere at resolutions (∼230 km) previously attainable only for short periods from ground-based observatories. A nearly fourfold increase in angular resolution from the existing space-based *SOHO*-Michelson Doppler Imager (MDI; Scherrer et al. 1995) magnetograms, as well as an increased sensitivity to weak magnetic fields has as one might expect, revealed the great complexity of the magnetic field at scales less than 1 Mm. For example, the emergence of bipolar ephemeral regions, a process which was thought to be fairly straightforward and well understood, has been shown by both observations and simulations to be much more complicated; instead of a single flux tube rising coherently through the surface, each bipole emerges as a mixture of magnetic features which gradually cancel, merge, and rearrange to form a coherent bipole (Cheung et al. 2008).

In the first paper in this series (DeForest et al. 2007, hereafter Paper I), we compared several magnetic feature-tracking algorithms, discussed the similarities and differences among them, and showed how some derived scientific quantities of interest are severely skewed by the choice of feature-tracking algorithm. In the previous paper in this series (Lamb et al. 2008, hereafter Paper II), we analyzed the methods of birth of features seen in MDI magnetograms. Consistent with the picture presented by Cheung et al. (2008) but at a much smaller spatial scale, the feature-tracking algorithm we employed found a dearth of true bipolar emergence events. Instead we found that, of all the magnetic features containing newly detected flux, the vast majority originated without another feature of either polarity nearby. We considered a competing model of asymmetric bipolar emergence, in which one pole of an emerging bipole is much larger and weaker than the other, thus evading detection. We ruled out this model and inferred that these "Appearing" features are manifestations of the aggregation of weak, previously existing flux into features large and strong enough to be detected in MDI. In this paper, aided by the availability of high-resolution space-based magnetograms from *Hinode*, we directly address this inference. We compare observed Appearances in a *SOHO*-MDI magnetogram sequence with the same area in a simultaneous, cospatial *Hinode*-Narrowband Filter Imager (NFI) magnetogram sequence. The higher angular resolution and increased sensitivity of the NFI magnetograms make them ideal for making this direct comparison.

The solar photospheric magnetic field is considered by some to be fractal in nature (Schrijver et al. 1992; Lawrence et al. 1993; Vishniac 1995; Nesme-Ribes et al. 1996). That is, the size distribution of magnetic fields makes it impossible to know the plate scale of a magnetogram just by inspection. Recent evidence of this fractal nature has been found by Parnell et al. (2009), who applied the "clumping" feature-tracking method to magnetograms at different times and at different resolution (MDI full disk, MDI high-resolution, and NFI magnetograms). Over nearly 6 orders of magnitude in flux (10^{16}–10^{22} Mx), they found that the probability distribution of flux in features is a power law with index $\alpha \approx -1.85$. This suggests, at least over this range in fluxes, a scale invariance of the distribution of magnetic fields that may well extend to even smaller fluxes beyond the current detection limit.

Because of this supposed fractal nature, processes which occur on more easily observable scales can be inferred to also occur on less easily observable scales, and thus there is value

in looking in detail at intermediate scales for the insight it may provide into smaller scales. The result of Paper II was made by ruling out a competing model; here, we confirm it by direct observation. We show here that roughly 75% of MDI-HR Appearances are due coalescence: the collection of diffuse flux from below the detection threshold into a smaller, stronger feature that can be detected in MDI. The remaining 25% are due to convergence of NFI features: the motion of multiple distinct NFI features toward each other that may result in the merging of the NFI features.

We then address the nature of the Appearances in *Hinode*-NFI magnetograms. We find that Appearances in NFI are also likely to be the result of the same phenomenon of flux coalescence and that the detected flux in these Appearances represents only about 50% of the total flux in the concentration. Hence, we conclude that the aggregation of weak flux due to flows plays a large role in the behavior of magnetic fields at scales of a few hundred kilometers.

We remind the reader (see the Paper I Glossary) that a "feature" is an observational term referring to a visually identifiable part of an image, while "flux concentration" is a localized cluster of magnetic flux which may consist of one or more features.

The paper is organized as follows: in Section 2, we describe the one MDI and two NFI data sets used in this paper and aspects of their preparation and the feature tracking performed on them. In Section 3, we show examples of Appearances in MDI and the associated data in NFI. Finding an objective metric to characterize the events was difficult, but there are sufficiently few that manual characterization is tractable. We extend the analysis used in Paper II to sub-arcsecond scales using the second, larger NFI data set. Finally, in Section 4 we discuss the implications of the results of this paper.

2. OBSERVATIONS

Three data sets are used in this analysis. The first two are simultaneous *SOHO*-MDI and *Hinode*-NFI magnetograms, used to confirm that Appearances seen in MDI correspond to real features at higher resolution. The third is a longer *Hinode*-NFI data set that enables us to investigate Appearances in the higher-resolution data. All three data sets were tracked using the SWAMIS feature-tracking algorithm (Paper I). For the MDI data set, we used the "downhill" method of feature identification, while the NFI data sets were tracked twice, once using the "downhill" method and once using the "clumping" method. The specific tracking parameters for each data set are given in Section 3.

2.1. MDI Data

The MDI data are an approximately 1 hr sequence of high-resolution ($0\farcs6$ pixel^{-1}) magnetograms taken near disk center on 2007 June 24, between 22:00 and 23:16 UT, covering an area $139'' \times 159''$. They were preprocessed in a manner similar to the preprocessing in Paper II. This included despiking to remove cosmic rays, compensation for radial projection, rotating to a common reference frame while preserving the native pixel size, temporal smoothing using a Gaussian kernel with an FWHM of 3 minutes, and spatial smoothing using a Gaussian kernel with an FWHM of 1 pixel. To facilitate comparison with the results of Paper II, it would be advantageous to prepare the data in exactly the same manner. However, this is not practical because of some key differences in the data set. First and foremost, temporal smoothing using a 12 minute FWHM Gaussian with a 5 minute cadence (as was done with the Paper II data set) would have an undesirable effect on this 76 minute data set, reducing it to only 15 frames. As the previous data set was nearly 24 hr long, greater temporal smoothing was not problematic. Similarly, since this data set's area is less than 10% of the previous MDI data set, we apply less spatial smoothing. The net effect is less noise reduction in this data set, but the analysis here does not require reducing the noise as much as the previous analysis due to the availability of simultaneous higher-resolution data. The noise in this prepared MDI data is $\sigma_{\rm MDI} = 9.5$ G, which led us to use thresholds of 28 and 38 G ($\approx 3\sigma$ and 4σ) in the feature tracking.

2.2. Simultaneous NFI Data

The second data set is a sequence of *Hinode*-NFI circular polarization filtergrams taken 200 mÅ blueward of the Na-D 5896 Å line center. The data have a 1 minute cadence from 2007 June 24 between 22:09 and 23:08 UT covering the same patch of the solar surface near disk center as the MDI data set. The spatial and temporal overlaps of these two data sets are key for understanding how much can be inferred from lower-resolution studies of the magnetic field.

At the time these data were prepared, calibrated magnetograms from the NFI were not available. The raw files are three-dimensional, two spatial dimensions and one polarization dimension. The size of the polarization dimension is 2: the first plane is the intensity (I) image and the second is the circular polarization (V) image. The flux density is proportional to V/I. Since there was no flatfield available in the 5896 Å passband, the only correction we applied was to remove the detector bias from the I image.[6] The values in the resulting V/I images ranged from approximately -0.04 to $+0.04$.

To roughly determine the range of the magnetic field measurements, we compared the NFI image from 22:34 to the average of five MDI images from 22:32 to 22:36. The pointing of the MDI image was taken to be definitive, and the pointing information in the FITS header of the NFI image was adjusted manually until it corresponded well with the MDI image. The NFI image was blurred with a 6 pixel half-width Gaussian to better match the MDI resolution, and both images were blurred again with a 12 pixel half-width Gaussian.

Finally, we plotted the values in the two images against each other as a scatterplot and found the best-fit line. The slope of this line was 6555 G and is the calibration factor that turns the V/I circular polarization maps into magnetograms. Formally, the calibration is expressed as

$$M = 6555\ \mathrm{G} \times \frac{V}{(I - 200 \times 2 \times N)}, \quad (1)$$

where N is the number of individual images taken in each polarization, is given by the FGNINT field in the FITS header of the image, and here is equal to 4. The factor of 2 comes from the addition of the right and left circular polarization images to create the I image, and 200 is an estimate of the detector bias added to each image (T. Tarbell 2008, private communication). Figure 1 shows the NFI and MDI images used to make the comparison, the comparison between MDI values and bias-subtracted NFI V/I image, and the difference between the calibrated NFI image and the MDI image.

[6] Later experiments using a more mature NFI data preparation pipeline showed little difference from or improvement upon the methods described here.

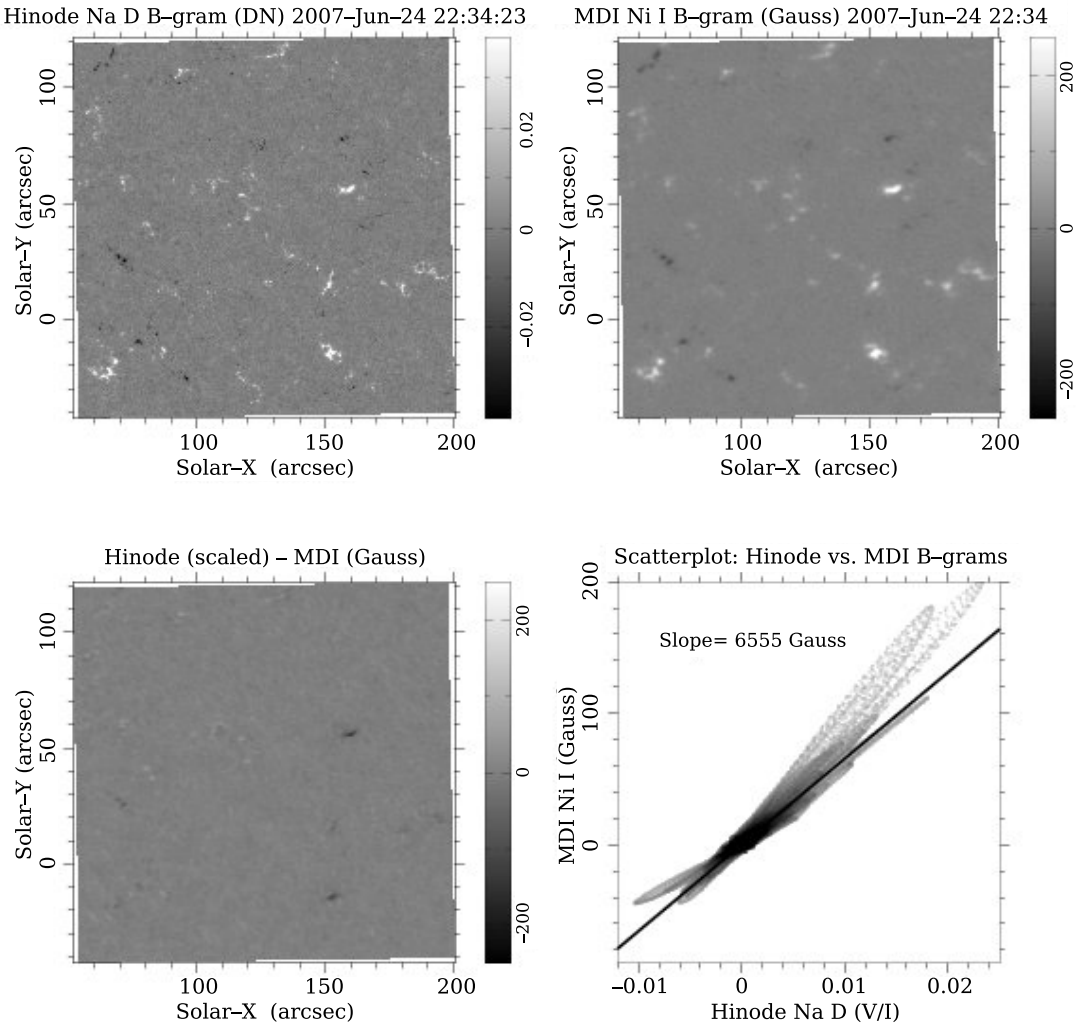

Figure 1. Clockwise from top left: *Hinode*-NFI Na-D 5896 Å V/I image from 2007 June 24, 22:34 UT; *SOHO*-MDI Ni-I 6768 Å high-resolution magnetogram from the same time; scatterplot of the values of the two images, showing the best-fit line having a slope of 6555 G; difference between the calibrated NFI and the MDI magnetograms.

Given that different spectral lines are used to create the MDI and NFI magnetograms, that these lines may have different formation heights in the solar atmosphere, and that the magnetic field at these heights may be different due to atmospheric stratification, it is possible that our cross-calibration contains some errors. However, extrapolating from Figure 6 in Metcalf et al. (1995), 200 mÅ from line center is mostly formed deep in the photosphere, so we do not expect this to be a serious problem. None of the results in this paper critically depend on our knowledge of the absolute field strengths, but this cross-calibration is useful for obtaining approximate physical quantities.

After the magnetograms were created, we applied the standard preprocessing steps: despiking to remove cosmic rays, derotation to a common reference frame,[7] temporal smoothing using a Gaussian kernel with an FWHM of 2 minutes, and spatial smoothing using a kernel

$$k = \frac{1}{16} \times \begin{bmatrix} 1 & 2 & 1 \\ 2 & 4 & 2 \\ 1 & 2 & 1 \end{bmatrix}, \quad (2)$$

which is equivalent to a truncated 3×3 Gaussian with an FWHM of 2 pixels. These temporal and spatial smoothing parameters were chosen after extensive experimentation in order to reduce the noise in this data set as much as possible. This prepared data set has also been used by Parnell et al. (2008), which required as low a noise level as possible. In the process of derotation, the spatial extent of the data set was reduced to 882×1012 pixels so that, to the extent allowed by the accuracy of the *Hinode* pointing information, no portion of the final field of view entered or left the data set during the 1 hr sequence.

As the last step of preprocessing, we applied a subsonic FFT filter to reduce the effect of p-modes and related noise. The effect of the filter was to eliminate any features traveling faster than the 7 km s^{-1} sound speed, as these are wave phenomena with high phase speed at the surface, rather than physical objects or flux concentrations. The Fourier-space filter was a truncated cone with apex at the origin and cone angle of 7 km s^{-1}. Sharp edges in a Fourier filter can introduce artifacts into the data, so the borders of the Fourier filter were smoothed. The cone boundary had a $\cos^2$ rolloff with a width of 2 km s^{-1} centered on 7 km s^{-1}. The cut plane of the cone had a $\cos^2$ rolloff with a width of 0.6 mHz centered on ± 1.7 mHz. High-speed, high-frequency components (those inside the truncated cone) were

[7] The derotation is not that important for NFI data, since *Hinode* tends to follow a patch of the solar surface as it rotates across the disk.

filtered out; all other components were left unchanged. Because the FFT filtering assumes that the data are periodic in time, aliasing between the beginning and end of the data set occurred. To eliminate this, the first and last frames were duplicated 5 times each to extend the data set in time and blended together smoothly with a $\cos^2$ rolloff. Edge effects in the spatial direction have been ignored. The temporal edge treatment is not perfect, and some artifacts do exist in the data because of it, but subsonic filtering removes visible *p*-mode patterns from the data set and reduces the rms noise by approximately 20% over the bulk of the data set. The noise in the final prepared NFI data was 6 G, and so we adopted thresholds of 18 and 24 G (3σ and 4σ) for the feature tracking.

2.3. Longer NFI Data Set

The final data set used in this paper is a long (5.25 hr) sequence of *Hinode*-NFI circular polarization filtergrams taken 188 mÅ blueward of the Na D 5896 Å line center. The data have a 45 s cadence from 2007 September 19 between 12:45 and 18:00 UT. After cropping to remove the portion of the image affected by the air bubbles inside the tunable filter (Tarbell 2007), the field of view is 1552 × 576 pixels, or 6.36 arcmin^2. This area is almost the same as the shorter NFI data set, but as we show in Section 3.2, the longer duration is necessary for studying the Appearances seen in NFI images. The center of the cropped field of view has coordinates of (14″,−228″), and the cosine of the angle between the disk center and the observer line of sight at that point is 0.97, so we do not expect significant line-of-sight effects in this data set. We created magnetograms from the circular polarization filtergrams using Equation (1). The *Hinode* NFI detector is comprised of two 2048 × 2048 detectors placed side-by-side to produce a 4096 × 2048 image, and these images are usually 2 × 2-binned on the spacecraft to produce a 2048 × 1024 image with 0.″16 pixels. The left detector suffers from a problem in which the median value of the columns in a magnetogram decreases toward the right edge of the detector (although occasionally a similar increase is present instead). This results in a large contrast across the chip border in the middle of the combined detector, as shown in Figure 2. This effect is not present in every magnetogram, and both the sign and magnitude of the effect vary when it is present. The cause of this problem is currently unexplained (T. Tarbell 2008, private communication).

Since the feature-tracking algorithm implicitly assumes that background noise is centered around zero for all parts of every image in the sequence, it is necessary to remove the spatially variable offset. Without this, weak features of one polarity would be missed, and a spuriously large number of features of the other polarity would be detected. To remove this effect, we have assumed that the offset is linear in position past a certain horizontal point.[8] We fixed this point at $x = 400$ pixels in the original 1728-column image (because of data rate considerations, occasionally only part of the detector is read out, usually symmetrically about the center of the combined detector). For each magnetogram, we found the median value for each column. We performed a linear fit to the median values in the range $x \in [0, 400]$ and a separate fit to the median values in the range $x \in [400, 863]$. We required that the fit is single-valued at the transition point $x = 400$. We subtracted this piecewise-linear fitted background from the input magnetogram and made no adjustment for the right half of the detector. With this adjustment, the contrast across the chip boundary is much reduced (Figure 2).

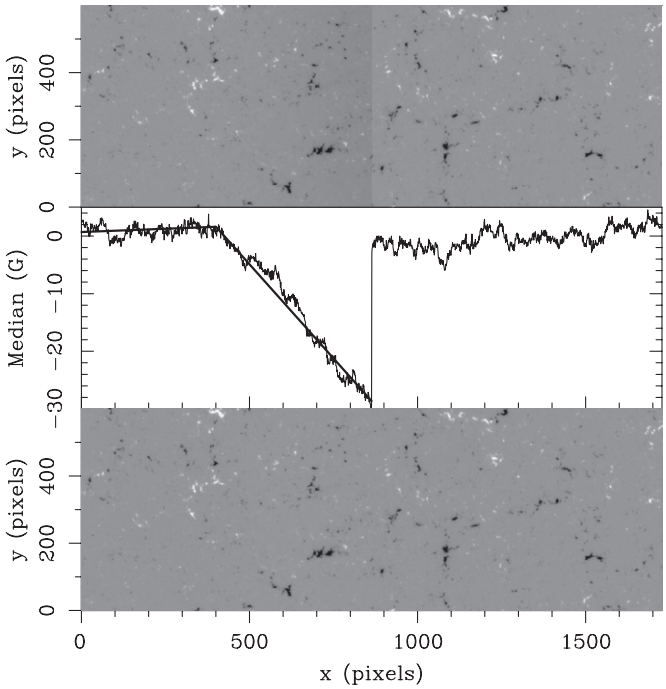

Figure 2. Example of the columnwise median offset in certain *Hinode* magnetograms. Top: original magnetogram, showing the large contrast (∼30 G) across the center of the chip. Middle: columnwise median across the magnetogram (solid line) and the best-fit constrained piecewise-linear fit on the left detector (dashed line). Bottom: corrected magnetogram showing the offset removed. The grayscale in both magnetograms saturates at ±300 G.

The magnetograms were then despiked to remove cosmic rays, derotated to a common reference frame in the middle of the data set, and temporally averaged using a Gaussian weighting. The temporal averaging function had an FWHM of 2 frames (1.5 minutes) and preserved the 45 s cadence of the original data. Finally, the magnetograms were spatially smoothed by convolving them with the kernel in Equation (2). The FFT filter, described for the 1 hr data set in Section 2.2, was not applied to this longer data set. Experiments showed that it did not have the same noise-reducing effect as on the short data set, and with no clear benefit it was not worth the possibility of introducing additional Fourier-related artifacts into the data. The reason why the FFT filter works on some data sets but not others is currently unknown but has been reported by others as well (T. Tarbell 2008, private communication).

3. RESULTS

3.1. Comparison of Simultaneous MDI & NFI Data Sets

In order to map MDI Appearance events to the corresponding location in the NFI images, it is necessary to align the images. Ideally, this could be easily accomplished using the pointing information in the FITS header of each image. The SOT image stabilization system (Shimizu et al. 2008) removes most of the high-frequency jitter from the image, but long-term pointing drift means the pointing information from NFI is not accurate enough to make this simple process viable.

Since only the relative pointing information and not the exact pointing information is relevant to the present work, it

[8] After this analysis, T. Tarbell (2008, private communication) stated that the offset may in fact be exponential in position instead of linear, but this has not been incorporated into the present work, and does not seem to bear on all of the data (such as the example presented in Figure 2).

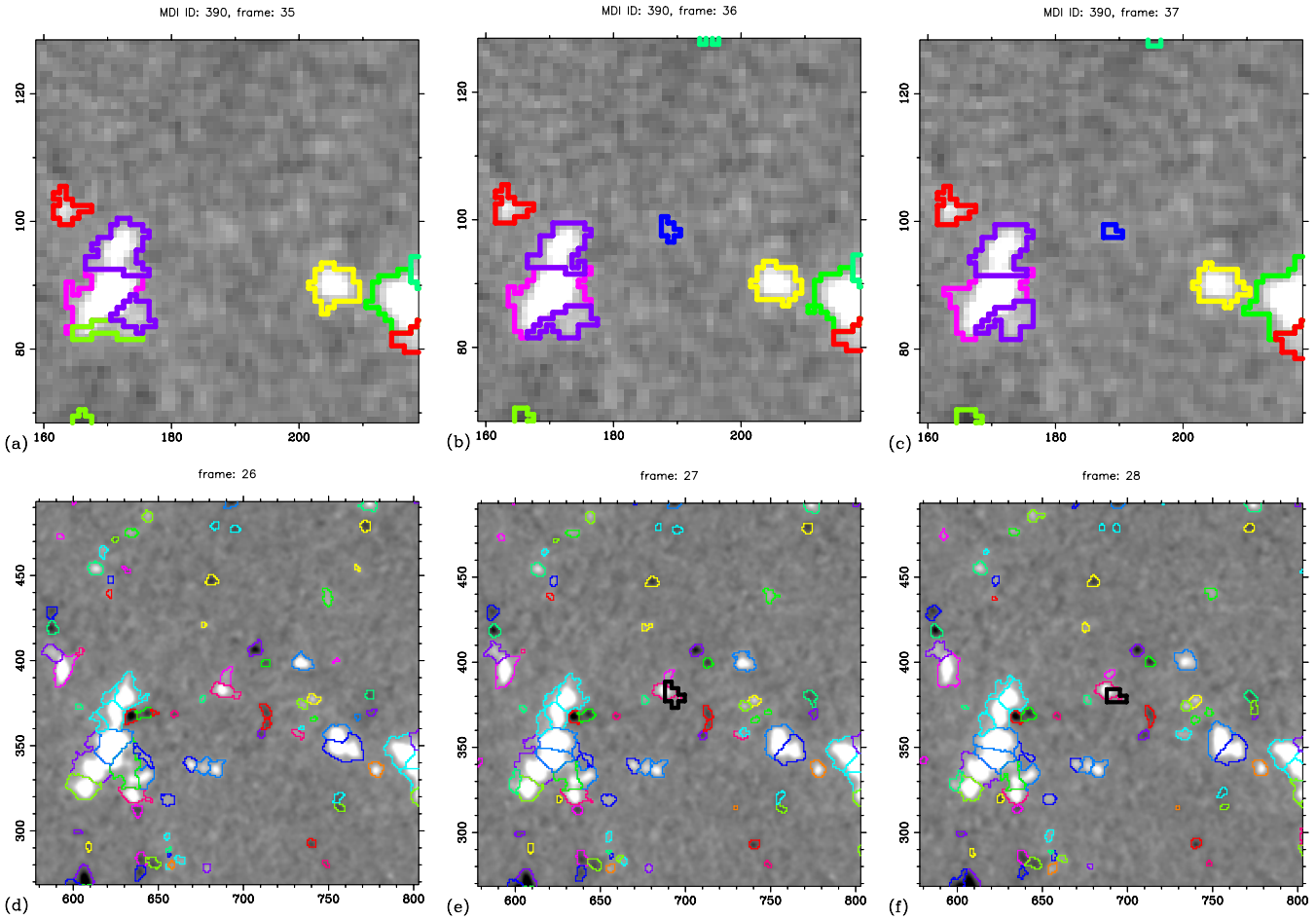

Figure 3. Panels (a)–(c): example of a feature (blue outline in the center of the middle and right panels) detected as an Appearance in *SOHO*-MDI data. Panels (d)–(f): the same region, at the same times, observed in *Hinode*-NFI. The outline of the Appearing feature in MDI is shown in black superimposed over the outlines of the other features identified by the downhill method.

(A color version of this figure is available in the online journal.)

is possible to perform the pixel-to-pixel alignment directly. We derived an image distortion map for each pair of simultaneous images. To do this, we identified every feature in both data sets that lived for the duration of the data set. We chose four features from that list, and we attempted (within the limits of the small sample) to choose features that were separated from other features and spaced across the field of view. The purpose of the first requirement was to isolate distinct flux concentrations. This reduced the influence of shifting intra-feature borders on the derived positions of the selected features. The purpose of the second requirement was simply to sample different portions of the field of view so that any local peculiarities of feature motions would not have a disproportionate effect on the co-alignment.

The co-alignment was performed after the tracking was completed, so we were able to use the centroid of each of these four selected features in both data sets as tie points to derive a two-parameter (linear), two-dimensional distortion mapping between the images. In general, a linear two-dimensional distortion mapping can contain skew terms, but we limited the mapping to independent scaling and shifting of the x- and y-axes. In this way, we are able to map the pixel coordinates in the MDI data set to pixels in the NFI data set for each frame. This mapping also automatically takes into account any residual *Hinode* pointing drift, since the drift is slow enough that features maintain their identity and are not affected by the mistaken identity problem (Paper I).

In the MDI data set, 669 features are found using the previously mentioned tracking thresholds of 28 G ($\approx 3\sigma$) and 38 G ($\approx 4\sigma$), the downhill feature identification method, a per-frame minimum size filter of 4 pixels, and a minimum feature lifetime of 4 frames. Of these, 121 are classified as an Appearance using a separation criterion of 5 MDI pixels (2.2 Mm). The average width ($\sqrt{\text{area}}$) of the Appearances is 2.3 pixels, which demonstrates that these features are well separated from other features compared to their size. We rejected from consideration the 27 features which were born before the start or after the end of the NFI data set, as well as the 6 features which map outside of the NFI field of view. We are thus able to analyze 88 MDI Appearances for correspondence in the NFI data sets. Figure 3 shows an example of the comparison between the downhill features identified in the two data sets. The middle column of panels corresponds to the birth time of the Appearing feature in MDI, and the left and right panels are one frame before and after. In the bottom row of panels, the location of the Appearing feature in MDI is outlined in black, showing a good overlap with two features in the NFI data. We can confirm that this is not a chance alignment because of the good alignment among the other flux concentrations which are present in both fields of view.

Not every correspondence between objects is as good as shown in Figure 3. This may be due to a combination of the imperfect nature of the image alignment, as well as the fact that

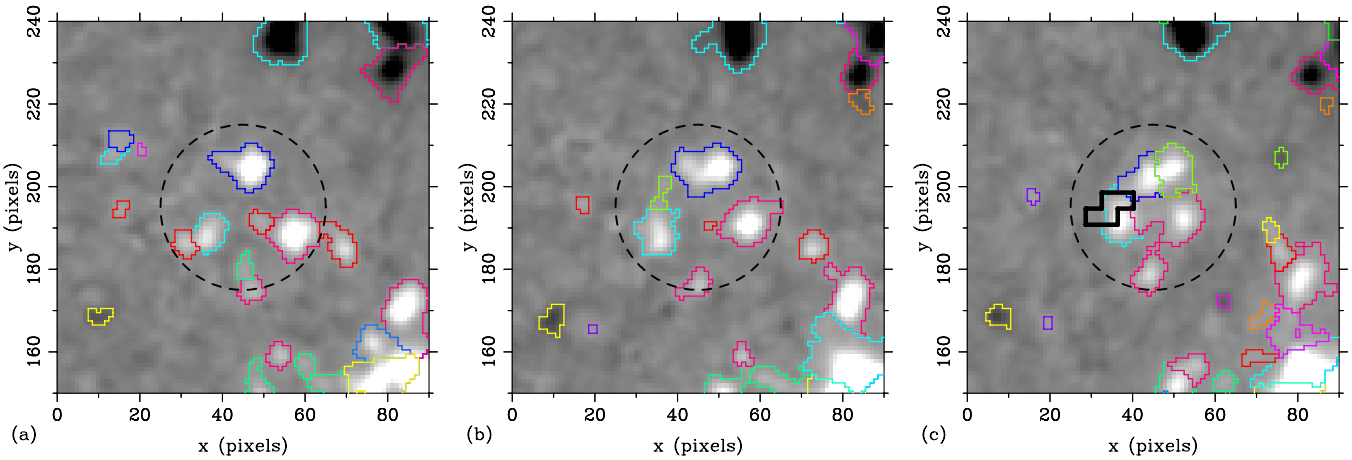

Figure 4. Clear example of convergence causing an MDI Appearance. The dashed circle highlights the region of interest. The blue, cyan, and magenta features begin moving toward each other. By the time of panel (c), the flux of the three previously distinct features is close enough to rise above the detection threshold in MDI and cause an Appearance (solid black outline in panel (c)). The frames are separated by 5 minutes.

(A color version of this figure is available in the online journal.)

the NFI field of view is on average 75% more feature dense than the MDI field of view. Therefore, there is a higher likelihood in NFI that a randomly chosen location will be near a detected feature, and so the feature corresponding to the MDI Appearance may by chance be near another feature. But deciding which feature(s) in NFI correspond(s) to the Appearing feature in MDI is not impossible. By dilating a mask of the MDI feature loci by just 1 MDI pixel, it is possible to find a correspondence between every MDI Appearance and at least one NFI feature. In this case, the features are those derived from the "clumping" algorithm, since the extent of features identified by that algorithm tends to be largely independent of the resolution of the data (Parnell et al. 2008, 2009).

Since every MDI Appearance event seen in this 1 hr sequence corresponds to at least one feature in the NFI data, and since most of these do not seem to be associated with a nearby feature of opposite polarity, a natural question to ask is: what is the behavior of the flux which causes the Appearance event in the MDI data? There are several possibilities. It is possible that some of the MDI Appearances correspond to an Appearance in NFI, but because of the observation that the MDI Appearing features all map to well-defined NFI features (and not weak ones), this can be largely ruled out. As in Paper II, it is possible that asymmetric bipolar emergence is responsible, but we again reject this scenario, this time using direct visual comparisons with the NFI data. They could correspond to the convergence of two or more distinct like-polarity features into close proximity. It was this scenario which was inferred in Paper II. Finally, they could correspond to the coalescence of a single relatively large, diffuse features in NFI into a smaller, stronger feature. We note that these last two possibilities are end points of a continuum of possible same-sign flux rearrangement scenarios.

Figure 3 shows that the situation is not as simple as we might like. Because of the constantly evolving boundaries and shape of the detected features, finding a metric by which to categorize the behavior of the features in NFI is not a simple task. For example, the area of a feature may both increase and decrease as the maximum flux in the feature steadily increases, even beyond the demise time of the Appearing feature in MDI. But movies of the evolution of the NFI features (from which the example in Figure 3 was extracted) provide more insight, and we find that both convergence and coalescence occur to produce the MDI Appearances. Figure 4 shows a clear example of multiple features converging over the course of 20 minutes to form an MDI Appearance (black outline in the last frame). Figure 5 shows a clear example of one concentration (consisting of three contiguous features) strengthening and shrinking to cause an MDI Appearance. In a subsample of the MDI Appearance events for which there was a clear correspondence between MDI and NFI features (61 of the 88 events), we found that 45 (approximately 75%) of the MDI Appearances could be attributed to coalescence of the NFI feature. Usually, the spatial distribution of the flux in NFI changes, giving the feature a higher mean field strength at approximately the same time that the MDI Appearance occurs. In the remaining 16 (25%), another feature converges on the location of an existing feature. As we noted above, both of these scenarios are primarily the rearrangement of flux. Coalescence rearranges flux within a single concentration, while convergence combines two or more features to form a single strong feature.

3.2. Appearances in NFI Data

If the Appearances in MDI can be shown using higher-resolution data to be due to coalescence and convergence of subresolution flux, what can the same technique that led to that inference in Paper II reveal about Appearances in the higher-resolution NFI data? In this section, we aim to determine the origin of the NFI Appearances by looking for surrounding flux that is below the detection threshold. We accomplish this by creating an ensemble average of the Appearances to search for a like-polarity halo. We find that it is not possible to do this with the shorter data set and that a longer data set is necessary.

3.2.1. Short NFI Data Set

In the simultaneous NFI data set, we find 2166 Appearances when using a 5 pixel separation criterion, as before. Of these, 1482 are initially "small" (area less than 10 pixels) and further than 5.8 Mm from the nearest edge of the field of view and so are appropriate to use in the ensemble averaging. This procedure, however, is susceptible to error from incorrect estimation of magnetograms' zero points.

The 2007 June 24 region under study does have more positive flux than negative flux as measured by both MDI and NFI.

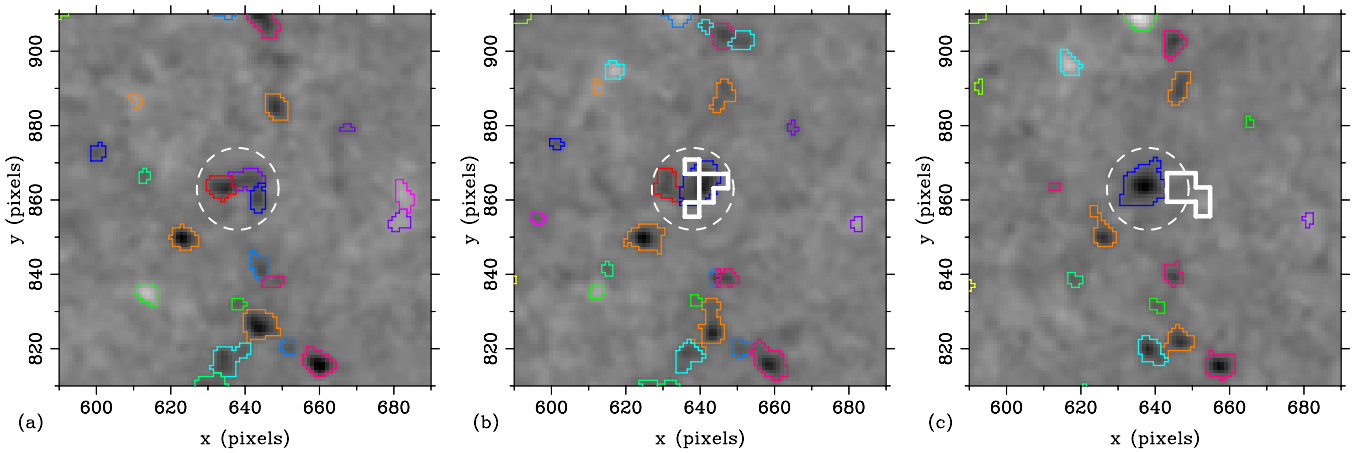

Figure 5. Clear example of flux coalescence. The dashed circle highlights the region of interest. The weak red, purple, and blue features in the center of panel (a) coalesce to form one strong feature in panel (c). Doing so causes an Appearance to occur in MDI (white outline in panels (b) and (c)). The offset of the two outlines in panel (c) is due to an error of 2–3 MDI pixels in the derived MDI-NFI image alignment. The frames are separated by 5 minutes.

(A color version of this figure is available in the online journal.)

The ratio ξ of average signed flux to average unsigned flux is +25% for the NFI data set. In a randomly selected NFI image (22:30 UT), the mean signed pixel value is +2.7 G, while the median value is −0.25 G. These mean and median values imply that the flux imbalance is due to pixels at the high end of the field strength distribution (presumably real, detected features) and is not due to an error in the zero-point calibration of the magnetograms.

When we consider all 1482 Appearances, the flux per unit radius $\frac{d\Phi(r)}{dr}$ shows the expected initial peak and descent corresponding to the detected feature, followed by a nearly linear increase at distances of 1–3 Mm. The linear increase could be attributed to a constant polarity background field, either due to an offset in the zero point of the magnetograms or due to an inherent flux imbalance in the region under study. However, the zero-point offset calculated from each magnetogram has been subtracted from each subimage prior to inclusion in the ensemble average image, so it is unlikely that this is still a major factor.

Figure 6 shows the flux profiles for the Appearances in the 1 hr NFI data set separated by polarity as well as the combined flux profile. There are 724 positive Appearances and 758 negative Appearances. Note that both profiles are positive at distances greater than ≈2 Mm, and although there are more negative Appearances than positive, the profile is steeper for the positive Appearances, leading to the net positive slope observed in the combined flux profile. This illustrates a subtle point regarding the sign homogenization; the sign homogenization will only cancel the net background field if equal numbers of positive and negative polarity events are used and if the average background field around the positive and negative Appearances (represented by the slopes in Figure 6) is the same. If either of these two conditions are not met, then a sign-homogenized ensemble average flux profile will display an increase at large distances (this was also seen in Figure 6 of Paper II).

The negative curve in Figure 6 displays a small negative plateau around 1 Mm which is not visible in the combined flux profile in that figure. This suggests that while the sign homogenization allows for an increase in the number of Appearances in the ensemble average and thus better statistics, it may also obscure features that correspond to real effects. In order to understand whether this plateau is real or not, and because the positive-polarity skew of the data set results from strong pixels that presumably are in detected features, it is necessary to increase the separation distance criterion that defines an Appearance. This allows us to study the average weak field in the vicinity of the Appearances without the influence of the stronger, detected features.

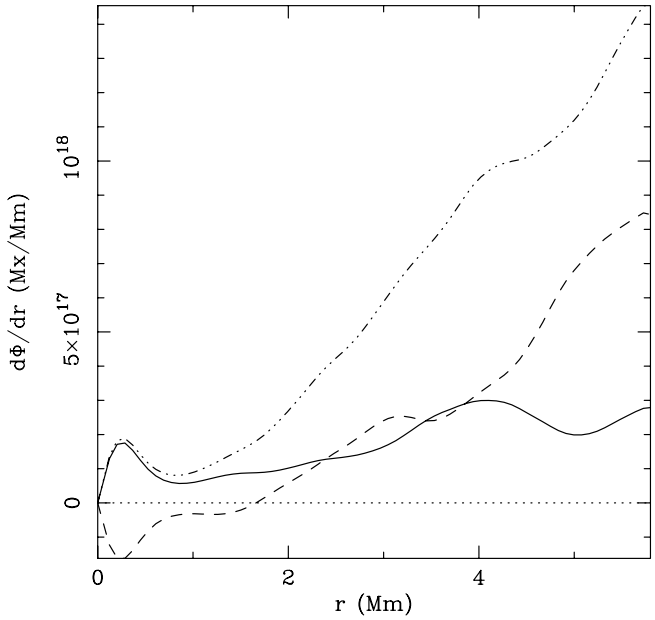

Figure 6. Flux profile of positive (dash-dotted line), negative (dashed line), and all (solid line) Appearances in the short NFI data set. Though more negative Appearances (758) occur than positive (724), the positive has a steeper slope at intermediate distances, allowing the positive curve to dominate the sign of the full ensemble profile.

Increasing the separation parameter reduces the number of Appearances available for inclusion in the ensemble average magnetogram. For example, increasing the separation criterion to 9 and 13 pixels reduces the number of usable Appearances to 856 and 451, respectively. Thus, it is necessary to determine the minimum number of magnetograms necessary before flux profiles do not change significantly between subsets of selected Appearances. We vary the number of Appearances in the ensemble average by selecting every nth Appearance, $n \in [20, 10, 5, 3, 2, 1]$, while ensuring that the samples are

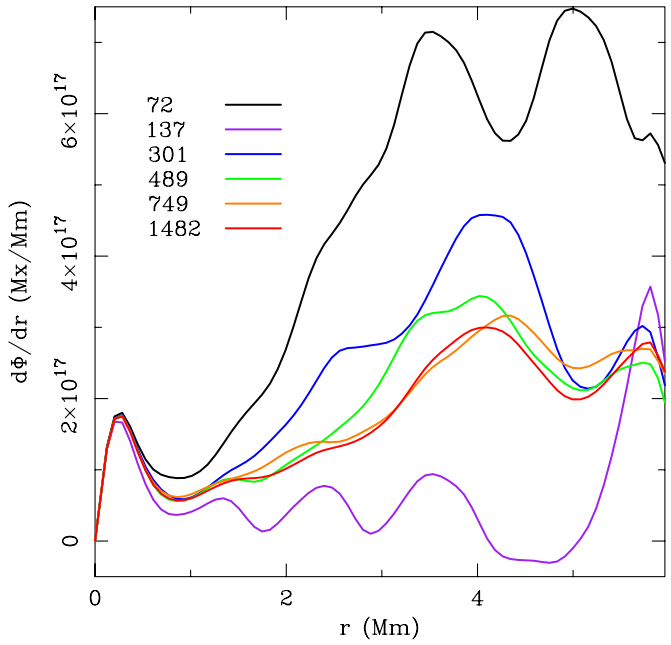

Figure 7. Flux profiles as a function of the number of averaged Appearances, from 72 Appearances (black line) to 1482 Appearances (red line). Aside from the initial rise and descent within 0.5 Mm, the profiles do not converge until over 700 Appearances are used (red and orange lines).

(A color version of this figure is available in the online journal.)

independent, especially for the smaller sets. In other words, the Appearances chosen for the $n = 20$ case are not a subset of those chosen for the $n = 10$ case, which are not a subset of those chosen for the $n = 5$ case. Figure 7 shows the result of using too few Appearances in the flux profile plots. The number of Appearances used are not exactly $\frac{1}{20}$th, etc. of the total number of Appearances because some are rejected for being too close to the edge of the field of view. We find that the flux profiles begin to diverge at $r \sim 0.5$ Mm, and only for $n \in [2, 1]$ do the profiles agree at all at larger distances. It is clear then that $\gtrsim$750 Appearances are necessary to reliably create the ensemble average magnetogram. Since only 1482 Appearances are found in the short data set, and since we would like to expand the separation criteria as much as possible, the longer NFI data set containing more Appearances is necessary.

3.2.2. Long NFI Data Set

In the long (5.25 hr) NFI data set, we find 112,217 features using tracking thresholds of 18 G ($\approx 3\sigma$) and 24 G ($\approx 4\sigma$), the downhill feature identification method, a per-frame minimum size filter of 4 pixels, and a minimum feature lifetime of 4 frames. Table 1 shows the number of Appearances as a function of the separation parameter s. Based on the analysis of the short NFI data set, $s = 13$ pixels is the limit above which the results of the ensemble averaging could not be trusted, but there are enough Appearances with $s = 13$ pixels to believe the flux profile has converged. We note that there is a competing effect which hinders our ability to work with large separation parameters. With a greater separation parameter, a greater portion of Appearances found by the event classification algorithm occur near the edge of the field of view. This is because the area searched by the event classification algorithm for an event right on the edge of the field of view is half that for a feature well inside the field of view, and so the probability of not finding a feature nearby (which defines an Appearance) increases near the edge of the field of view. This factor of 2 is only a lower limit; because of corners, the factor is typically closer to 4. Since we reject Appearances that are closer to the edge of the field of view than the half-width of our extracted magnetogram subimage, this severely constrains the number of Appearances available to create the composite Appearance magnetogram. Table 1 suggests that while using $s = 13$ pixels would produce reliable results in the ensemble averaging, using 20 or even 15 pixels would result in too few good Appearances to be reliable.

Table 1
Number (N) of Appearances in the Long NFI Data Set as a Function of the Separation Parameter s (in pixels and in Mm)

s (pixels)	s (Mm)	N	$N_G(4.1)$	$N_G(5.8)$
5	0.58	10909	8818	8087
10	1.16	4436	3398	3087
13	1.51	2403	1740	1554
15	1.74	1529	1055	926
20	2.32	497	291	253

Notes. Since producing the ensemble images requires that the individual subimages do not contain pixels outside of the field of view, the number of "good" events N_G for image half-sizes of 4.1 and 5.8 Mm, respectively, are also shown. In all cases, only those Appearances having an initial size $\leqslant 10$ pixels were used.

In this data set there is a negative flux imbalance, and it too is a result of features at the large end of the flux distribution. In a sample magnetogram chosen randomly from the data set, the flux imbalance in all pixels less than $1\sigma = 6$ G (i.e., those pixels assumed to be noise) is only $\xi_{<1\sigma} = +0.9\%$. But when only considering values greater than $3\sigma = 18$ G, the flux imbalance is $\xi_{>3\sigma} = -35\%$. When considering all pixels, the value is $\xi_{\rm all} = -26\%$.

Figure 8 shows flux profiles for the ensemble averages of the positive and negative Appearances separately as well as together. Note that in both the positive and negative cases, there is a large increase in negative polarity flux (cf. opposite polarity) at distances larger than approximately 3.5 Mm. When the sign of the magnetograms is reversed for the negative Appearances, the greater number of these results in a positive bias to the combined ensemble average at distances greater than 3.5 Mm.

The central plateau for which there was some evidence in the short NFI data set is much more evident now that a larger separation criterion has been used. It extends out to $\approx$2.5 Mm for the positive Appearances and to $\approx$3.3 Mm for the negative Appearances. This plateau exists for both the positive and the negative Appearances separately and has the same sign as the detected features. This suggests that there really does exist a like-polarity halo of undetected flux around the detected Appearing feature. Combined with the MDI-NFI results of Section 3.1, it implies that coalescence of this diffuse halo is responsible for the Appearance events seen in NFI magnetograms.

If the Appearances observed in NFI are also the coalescence of weak flux into a feature large enough and strong enough to detect, it is useful to have an estimate of the fraction of flux that goes undetected by the instrument and tracking algorithm, i.e., the ratio of the flux in the core to the flux in the extended halo. By modeling the flux profiles of the core and the background field, we can measure the component in the halo. We model the core as a two-dimensional Gaussian and the background field as a two-dimensional logarithm with an inner cutoff. The logarithmic formulation ensures that this profile is a straight

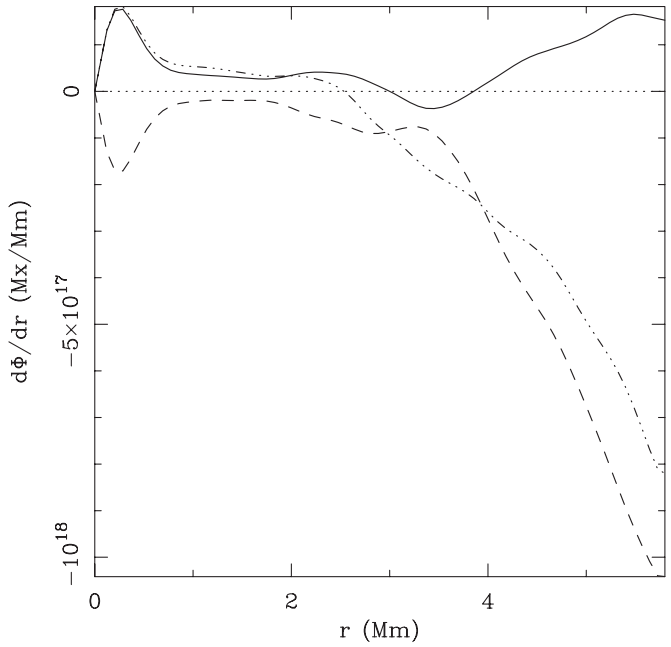

Figure 8. Flux profiles for the positive (dash-dotted line; $N = 742$) and negative (dashed line; $N = 812$) Appearances separately, as well as combined (solid line; $N = 1554$), as identified in the long NFI data set.

line with an intersection not at the origin. Mathematically, the components are

$$B_G(r) = c_1 \exp\left(-\frac{r^2}{2c_2^2}\right) \tag{3}$$

$$B_L(r) = \begin{cases} 0 & r \leqslant c_3 \\ -c_4 \ln\left(\frac{r}{c_3}\right) & r > c_3. \end{cases} \tag{4}$$

Table 2 lists the coefficients for a manual fit of the model to the flux profiles for both the positive and negative Appearances, and Figure 9 shows the resulting two-component model and the comparison to the data.

Recent calculations of the *Hinode*-SOT-BFI (DeForest et al. 2008) and NFI point-spread functions (PSFs) indicate that deconvolution of NFI magnetograms is important for recovering substructure lost by unavoidable imperfections in the telescope optics. Without deconvolution, features seem weaker and more spatially extended than they really are. A natural consequence of this might be the observed halo of weak flux around the detected features. While deconvolution has not been performed on the raw data used in this paper, we have deconvolved the images of the ensemble average of Appearances in order to differentiate between spreading of the magnetic signal by the telescope and natural spreading of the feature itself. Since convolution is distributive, operating on the ensemble average is the same as operating on the raw data and is also more convenient. The bottom row in Figure 9 shows the flux profiles that result from deconvolving the ensemble average Appearances and their resultant model fit. In general, one sees that the Gaussian component is stronger and more narrowly peaked as expected and that the parameters controlling the $\ln(r)$ component are not strongly affected by the deconvolution.

To estimate the fraction of non-detected flux in each Appearance, we calculate the total flux in the ensemble average that occurs within the circle before the negative polarity background begins (i.e., for $r < c_3$) and compare it to the flux in the Gaussian core of the Appearances. The fraction of the total flux not accounted for by the Gaussian core is also listed in Table 2 and is approximately 50% for most cases.

Table 2
Coefficients for the Empirical Two-component Model of Appearances for Both Positive and Negative Appearances, and Using the Original and Deconvolved Data

Flux Profile	c_1 (G)	c_2 (px)	c_2 (Mm)	c_3 (px)	c_3 (Mm)	c_4 (G)	Missing
+	20.5	2.1	0.24	21	2.4	−2.4	51%
+ (deconv)	35	1.8	0.21	21	2.4	−2.5	47%
−	−20	2.1	0.24	28	3.2	−5	62%
− (deconv)	−34	1.8	0.21	29	3.4	−6	52%

Notes. c_1 and c_4 are in gauss, c_2 and c_3 are given in pixels, and Mm for convenience. The column labeled "missing" indicates the fraction of flux interior to the logarithmic background NOT represented by the Gaussian core, as described in the text.

Some methods for feature identification not used in this paper (Strous 1994; Hagenaar 1999) only identify the flux in the convex core of the feature. Assuming a Gaussian flux density distribution, the "true" flux of the feature is calculated by multiplying the detected flux by a factor of 2.5. As we showed in Paper II, the flux profile of a two-dimensional Gaussian peaks at $r = \sigma$ and all of the models in Figure 9 agree very well with the data up to this point. This is also the location where the concavity changes sign. So, the factor of 2.5 used in the curvature-based methods will account for the Gaussian component of these Appearing features. But since the flux profile of the ensemble average of these features falls off more slowly than the Gaussian, Table 2 suggests that total flux in at least the smallest features found with a curvature-based method should be increased by another factor of approximately 2. Whether this flux profile behavior is common for much stronger features (and thus the additional factor of 2 is necessary for those as well) is beyond the scope of the present work. We note that the downhill-threshold feature identification method used in this paper makes no assumption about the "true" flux in a concentration and so is not directly affected by the additional factor of 2.

Deconvolution also shows that the left side of the NFI field of view suffers from an as-yet unexplained "glint" which causes features to have a nearby ghost feature. Since the ghost feature is always the same distance (a few pixels) and orientation (to the lower-right) from the real feature, and since it is not present in the center and right sides of the image, we can confidently assume that it is an artifact of the telescope optics and not a product of the deconvolution. The deconvolution just makes the ghost feature visible. Since we have not used deconvolved data here, the ghost feature manifests mainly as an asymmetric extension of the real feature, meaning the feature will be slightly larger in one direction than it would be if it were only due to its natural extent and the telescope PSF blurring. Because the ghost feature is not well separated from the real feature, we expect it to have little effect on the results presented here.

3.3. Flux Imbalance in the Data and Appearing Features

As noted earlier, all of the data sets used in this paper have a significant flux imbalance. In all three data sets, the imbalance is due to strong features and not to a systematic bias in the magnetogram zero point. In addition to the statistics quoted previously, this can be seen in Figure 10. To calculate the imbalance as a function of field strength for each data set in Figure 10, a histogram was made of all of the positive and negative pixel values in every frame of the data set, using 5 G

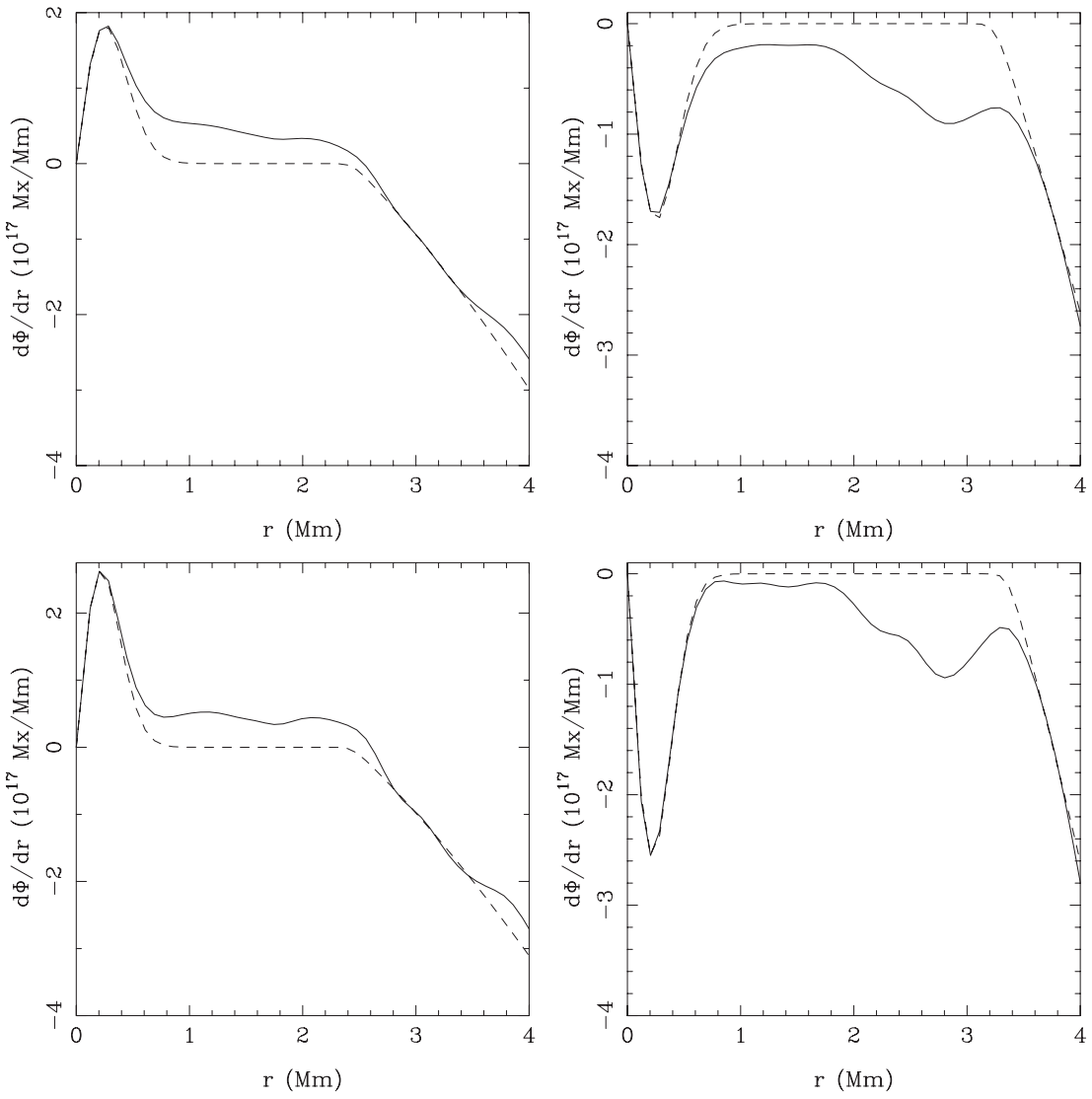

Figure 9. Flux profiles (solid line) for the positive (left column) and negative (right column) Appearances, using both original (top row) and deconvolved (bottom row) ensemble averages. A two-component model (dashed line) consisting of a Gaussian core and a negative polarity logarithmic background is also shown. The fitting parameters are listed in Table 2.

bins. The imbalance was calculated for each bin as

$$\xi = \frac{n_p - n_n}{n_p + n_n}, \tag{5}$$

where n_p and n_n are the number of positive and negative pixels in each bin, respectively. The Appearances found in each data set also exhibit a sign imbalance, when calculated as in Equation (5), but setting n_p and n_n to be the number of positive and negative Appearances in the data set. The Appearance sign imbalances for the data sets are 14% (MDI), −2% (short NFI), and −5% (long NFI). These imbalances are much smaller than the flux imbalances of the data sets in general. Since Appearances are initially detected as weak features just above the lower detection threshold, it is also useful to compare their sign imbalance to the sign imbalance of the data sets at that threshold. The vertical lines of Figure 10 mark the lower detection thresholds for the data sets. The imbalance of the data sets at the lower thresholds is much larger than the imbalance of Appearances. This shows that Appearances are nearer more nearly polarity-balanced than would be expected from features chosen randomly from the data set. We discuss this further in the final section.

4. DISCUSSION

In this paper, we have continued our investigation of small-scale apparent unipolar flux emergence events (Appearances) seen in solar magnetograms. We have shown that every Appearance in the MDI data set which is not affected by spatial and temporal edge effects has at least one corresponding feature in the NFI data set. This directly confirms that the Appearances found in Paper II are *real flux concentrations* and not some chance noise fluctuation.

In about 75% of cases for which a human judgment can be made, the Appearance is due to the reorganization of flux within a single flux concentration, a possibility not explicitly considered in Paper II. In the remaining 25% of cases, two or more distinct features come together to form a larger, stronger feature, which was the expected result from Paper II. One should keep in mind, however, that this determination was made by eye, since we did not develop an algorithm that could discriminate between the two.

As one might expect, the feature-tracking algorithm still finds Appearances in the higher-resolution *Hinode*-NFI magnetograms. By using a large data set, we are able to select

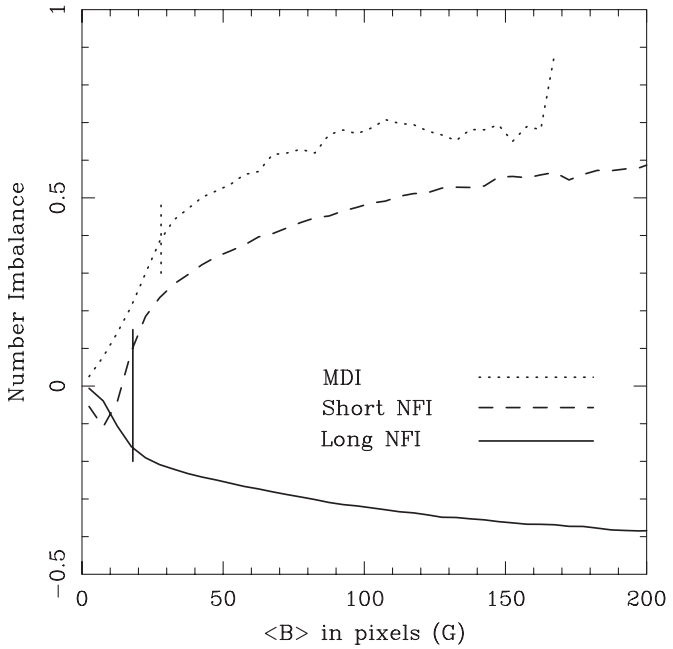

Figure 10. Flux imbalance as a function of field strength for all three data sets used in this paper. The method of calculating the imbalance is given in the text. The short vertical lines mark the lower detection thresholds for the MDI (dotted) and NFI (solid) data sets.

those Appearances that have no other magnetic features within 1.74 Mm. This allows us to create an ensemble average of the Appearance events while reducing the effect of the region's overall flux imbalance. The resulting ensemble average has three components. At the center is a Gaussian profile, representing the Appearing feature itself. At a distance of about 1 Mm, a weak like-polarity halo begins. At a distance of approximately 2–3 Mm, the negative polarity background of the region begins to dominate.

Three points taken together suggest that a similar process produces both the MDI and the NFI Appearances: that Appearances observed in MDI data are always associated with at least one well-defined feature in the higher-resolution and more sensitive NFI data; that the NFI feature usually seems to be contracting around the time of the MDI Appearance; the presence of a weak like-polarity field around the ensemble average of NFI Appearances. We therefore find it likely that NFI Appearances are also produced by the coalescence of weak, broadly distributed subresolution flux into features strong enough to detect with the feature-tracking algorithm.

If Appearances in the NFI data are largely due to coalescence of flux that had previously been too dispersed to be detected, then the amount of flux in the halo can give some insight into the total flux of the source concentration. For the positive and negative Appearances, both with and without deconvolution, we have produced a model comprising a Gaussian core and logarithmic negative polarity background. By comparing the detected flux interior to the distance at which the background becomes important with the flux in the Gaussian core, we have estimated the amount of "missing" flux in the Appearances. Approximately 50% of the total flux in the weak flux concentration is missing from the detected Appearances.

Our current work suggests that the process is at least to some extent scale invariant, so it is natural to ask over what range of scales this process of flux coalescence occurs? It is clear that with sufficiently poor resolution, the formation of network concentrations at the supergranular borders may look like Appearing flux (Smithson 1973). But at higher resolution, the answer is not as clear. The difference between the MDI and NFI resolution (as indicated by the pixel size) is a factor of 3.75. A similar increase in resolution beyond NFI would result in 0.″04 pixels yielding (neglecting the telescope PSF) better than 0.″1 resolution. However, we quickly run out of known surface flows which may coalesce the flux on these scales—below the scales of granulation, the observed energy spectrum of the vertical velocity field drops rapidly (Rieutord et al. 2010).

If there is no smaller-scale surface flow than granulation, and if the *G*-band bright points, filigree, and ribbons observed at 0.″1 resolution by Berger et al. (2004) really do represent fundamental units of flux on the Sun, then it is not unreasonable to expect that feature Appearance will all but disappear in high-resolution magnetograms taken with the future Advanced Technology Solar Telescope (Rimmele et al. 2001). However, if features do continue to Appear at even these scales, we must question whether emergence of kilogauss-strength isolated, monolithic flux tubes is a reality on the solar surface or whether it is just a useful tool for thought experiments.

Can the polarity imbalances shed more light on the origin of the observed flux? We would like to know whether the flux in Appearances is new (i.e., produced by a granulation-scale dynamo) or old (i.e., broken down from existing features). We make two assumptions: that any flux produced by a granulation-scale dynamo is balanced, and that the origin of any polarity imbalance would be due to remnant active region or other large-scale fields.

First, we note that the observed relation between polarity imbalance and field strength could be obtained if a background field exists (regardless of origin), if flux emerges balanced on some range of small scales, and if that emerging flux accumulates to form the features we observe. The accumulation of flux into features may be thought of as a series of positive and negative increments in flux. Since strong features will have required more samples of the biased field than weak features, they will tend to the polarity of the background field and could produce the observed distribution.

Conversely, the observed imbalance-field strength relation could be obtained from large-scale fields cascading downward in spatial scale. This is because as the strong fields are fragmented and weakened, the number of pixels in a given scene that are in those smaller field strength bins increases. Since the weaker non-remnant fields are presumably balanced, the total polarity imbalance in the weak field strength bin is smaller than in the stronger field strength bin. In the present work, we cannot distinguish between these two scenarios without more information on how long a given active region influences the area into which it disperses, or how common random-walk flux accumulation is in producing features in the magnetic network.

It is tempting to compare the polarity imbalances of the Appearances and the whole scene, observe that the polarity of the Appearances is more balanced than would be expected, and conclude that they have a different source than the background field. However, that ignores the fact that that is a comparison between newly-detected flux and flux in features with a mixture of lifetime phases. A more rigorous comparison might be between the polarity imbalance of Appearances at two different spatial scales (i.e., MDI and NFI). While the imbalance of the Appearances in the short NFI data set is smaller than the imbalance of the Appearances in the MDI data set, we also note that the

detection threshold for the short NFI data set is lower (assuming that our calibration constant is approximately correct). Without a systematic study involving several paired MDI and NFI data sets using the same feature detection thresholds, it is unclear whether the more balanced NFI Appearances are a real effect or a product of our calibration or detection thresholds.

The authors thank T. Tarbell for discussions regarding the NFI calibration and help in selecting suitable data sets. This work was supported by NASA grant NX08AJ06G (SHP-GI program). The authors thank the *SOHO*-MDI and *Hinode* teams for making their data publicly available. *SOHO* is a project of international collaboration between ESA and NASA. *Hinode* is a Japanese mission developed and launched by ISAS/JAXA, with NAOJ as domestic partner and NASA and STFC (UK) as international partners. It is operated by these agencies in co-operation with ESA and NSC (Norway).

REFERENCES

Berger, T. E., et al. 2004, A&A, 428, 613
Cheung, M. C. M., Schüssler, M., Tarbell, T. D., & Title, A. M. 2008, ApJ, 687, 1373
DeForest, C. E., Hagenaar, H. J., Lamb, D. A., Parnell, C. E., & Welsch, B. T. 2007, ApJ, 666, 576
DeForest, C. E., Lamb, D. A., Berger, T. E., Hagenaar, H. J., Parnell, C., & Welsch, B. T. 2008, in AGU Spring Meeting Abstracts, D1
Hagenaar, H. J. 1999, PhD thesis, Utrecht Univ.
Kosugi, T., et al. 2007, Sol. Phys., 243, 3
Lamb, D. A., DeForest, C. E., Hagenaar, H. J., Parnell, C. E., & Welsch, B. T. 2008, ApJ, 674, 520
Lawrence, J. K., Ruzmaikin, A. A., & Cadavid, A. C. 1993, ApJ, 417, 805
Metcalf, T. R., Jiao, L., McClymont, A. N., Canfield, R. C., & Uitenbroek, H. 1995, ApJ, 439, 474
Nesme-Ribes, E., Meunier, N., & Collin, B. 1996, A&A, 308, 213
Parnell, C. E., DeForest, C. E., Hagenaar, H. J., Johnston, B. A., Lamb, D. A., & Welsch, B. T. 2009, ApJ, 698, 75
Parnell, C. E., Deforest, C. E., Hagenaar, H. J., Lamb, D. A., & Welsch, B. T. 2008, in ASP Conf. Ser. 397, First Results from Hinode, ed. S. A. Matthews, J. M. Davis, & L. K. Harra (San Francisco, CA: ASP), 31
Rieutord, M., Roudier, T., Rincon, F., Malherbe, J., Meunier, N., Berger, T., & Frank, Z. 2010, A&A, 512, A4
Rimmele, T. R., Keil, S. L., Keller, C. U., & Hill, F. 2001, in AGU Spring Meeting Abstracts, 31
Scherrer, P. H., et al. 1995, Sol. Phys., 162, 129
Schrijver, C. J., Zwaan, C., Balke, A. C., Tarbell, T. D., & Lawrence, J. K. 1992, A&A, 253, L1
Shimizu, T., et al. 2008, Sol. Phys., 249, 221
Smithson, R. C. 1973, Sol. Phys., 29, 365
Strous, L. H. 1994, PhD thesis, Utrecht Univ.
Tarbell, T. D. 2007, SolarNews, http://spd.aas.org/SolarNews/archive/news.2007/21.nov
Tsuneta, S., et al. 2008, Sol. Phys., 249, 167
Vishniac, E. T. 1995, ApJ, 446, 724